Design of an Electromagnetic Setup for Independent Three-Dimensional Control of Pairs of Identical and Nonidentical Microrobots

Federico Ongaro, Stefano Pane, Stefano Scheggi, and Sarthak Misra, *Member, IEEE*

***Abstract*—Independent control of microrobots is a cardinal challenge for manipulation at micro/nano scale. In this paper, we design and assemble an electromagnetic setup to overcome some of the major obstacles in the independent control of microrobots. The demanding magnetic requirements are met by the presented experimental testbed that is able to produce magnetic fields and gradients of, respectively, 160 mT and 3.6 T/m at the center of the workspace. Through the design process of this testbed, we analyze the importance of design parameters and derive a quantitative analysis of the requirements for the dissipation of the generated heat. Further, we present and develop the model and software infrastructure, capable of running at 25 Hz, necessary for independent control of multiple microrobots. We also introduce two novel techniques for current-minimizing mapping of the desired forces into currents at the electromagnet. Finally, the capabilities of the setup are demonstrated through independent control of two, both identical and nonidentical, soft-magnetic microspheres in three-dimensional space—with average root mean square errors of 102 μm and peak velocities of up to 331 μm/s.**

***Index Terms*— Medical robotics, motion control, multi-robot systems.**

I. Introduction

In RECENT years, microrobotic devices have drawn a lot of interest, mainly due to their great potential to enhance the functionality of micromanipulation in medical, biological, chemical, and industrial environments. Being small and untethered, microrobots have the potential to drastically improve the effectiveness of various tasks, such as targeted drug delivery, particle separation, mixing, pumping, assembly, manipulation, microsurgery, and chemical analysis [1]–[5].

However, constrained by their small size, these robots are often bound to rather simple and passively actuated structures [6], [7]. Thus, their ability to exert strong forces and perform complex tasks is typically limited. Endowing microrobots with the ability to cooperate, would therefore, allow these robots to overcome this major drawback—without requiring any cumbersome additional structure. Microrobots could maintain the agility and flexibility provided by their microscopic size, while also being able to perform elaborate tasks, with high strength requirements, in hard-to-reach environments. Effectively, cooperative microrobots might open the way to a whole new set of challenges and tasks, such as swarm manipulation of large objects that are currently precluded from robotics at the microscale.

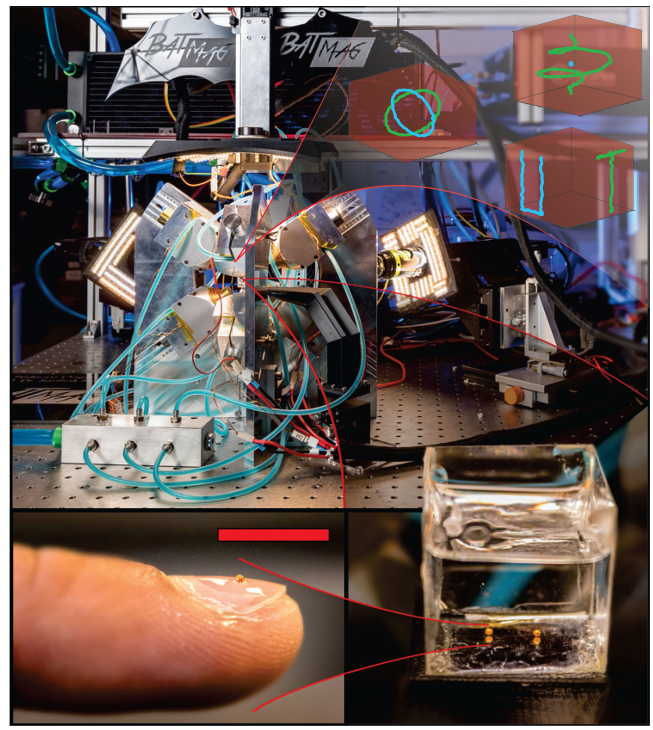

Fig. 1. Electromagnetic setup (BatMag). *Top-right inset*: Representative paths simultaneously followed by the microspheres. *Bottom-right inset*: A detail of the workspace with the glass cube and two micro-spheres (radius: 350 μm). *Bottom-left inset:* A detail of a microsphere (radius: 350 μm) positioned on top of a fingernail. Scale-bar: 8 mm.

Manuscript received May 30, 2018; revised July 13, 2018; accepted October 1, 2018. Date of publication November 6, 2018; date of current version February 4, 2019. This paper was recommended for publication by Associate Editor Jake Abbott and Editor Pierre Dupont upon evaluation of the reviewers' comments. This work was supported by the European Research Council under the European Union's Horizon 2020 Research and Innovation programme under Grant #638428—project *ROBOTAR*: Robot-Assisted Flexible Needle Steering for Targeted Delivery of Magnetic Agents. *(Corresponding author: Federico Ongaro.)*

F. Ongaro, S. Pane, and S. Scheggi are with the Surgical Robotics Laboratory, Department of Biomechanical Engineering, University of Twente, Enschede 7522 NB, The Netherlands (e-mail: f.ongaro@utwente.nl; stefa.pane@gmail.com; stefano.scheggi@gmail.com).

S. Misra is with the Surgical Robotics Laboratory, Department of Biomechanical Engineering, University of Twente, Enschede 7522 NB, The Netherlands, and also with the Department of Biomedical Engineering, University of Groningen and University Medical Centre Groningen, Groningen 9713 GZ, The Netherlands (e-mail: s.misra@utwente.nl).

This paper has supplementary downloadable material available at http://ieeexplore.ieee.org, provided by the author.

Color versions of one or more of the figures in this paper are available online at http://ieeexplore.ieee.org.

Digital Object Identifier 10.1109/TRO.2018.2875393

Given the major significance of such breakthrough, numerous studies have discussed viable techniques for its realization. In particular, acoustic tweezers have drawn attention for such application [8]. Nonetheless, this method demands establishing standing-wave-based pressure traps, which are challenging to achieve in *in-vivo* environments. Conversely, optical tweezers (high-intensity laser beams) do not suffer from this limitation, and have been widely used for control of microrobots [9]–[11]. However, high-intensity lasers are pernicious to human cells and, due to their high-frequency, cannot penetrate the opaque human body. Contrastingly, humans are transparent to quasi-static magnetic fields. Additionally, human exposure to magnetic fields has been proven safe even at high intensities [12]. Thus, such fields are a widely diffused choice for motion control of magnetic microrobots.

Even so, independent magnetic control of microrobots still presents relevant challenges [13]. Arguably, the major of these is that all the manipulated robots receive the same control inputs. Further, the coupling of these control inputs is nonlinear with respect to both space and magnitude of the inputs. Three main strategies have emerged to address these issues, which are as follows.

1) The use of microrobots that differ in shape or magnetic properties. Due to this difference, the robots (or their components) behave differently when exposed to a homogeneous magnetic field [14]–[17].
2) The use of specialized substrates, such as electrostatic braking pads or arrays of microcoils, that selectively activate/deactivate robots in specific areas [18], [19].
3) Exploitation of the magnetic field and gradient inhomogeneity for independent control [20]–[22].

Each one of these techniques has its following advantages and limitations.

1) Specifically, the first technique provides a reliable control of upto eight-degrees of freedom (DOF). However, it requires precise modeling and prevents the control of robots exhibiting comparable magnetic response. Moreover, this technique is often based on the average of several control inputs over a period of time, effectively limiting the control bandwidth.
2) On the other hand, the second technique offers very high control frequencies, complete decoupling of the inputs, and numerous DOF. Yet, this technique relies on the proximity of the robots to a large and tethered substrate, hindering its application in hard-to-reach or three-dimensional (3-D) environments.
3) Finally, the third technique allows to steer both identical and nonidentical microrobots with virtually no constraint on the number of DOF. Nonetheless, this technique revolves around the solution of a nondeterministic polynomial-time (NP) nonconvex problem, and thus requires a significant computational effort. Moreover, this technique has so far only been successfully implemented in two-dimensional (2-D) gravity-neglecting environments.

This 2-D-space limitation is not only due to the NP complexity, but also due to the technical requirements. A microrobot constrained along its gravitational axis, and moving in a flow-less 2-D environment, is essentially inert. Therefore, even minuscule forces generated by weak magnetic fields result in its motion. Conversely, in the 3-D-space, gravity has to be continuously compensated, requiring a constant, significant, force output. During magnetic control, this force has to be generated by strong magnetic fields and gradients. Furthermore, the strength of these fields increases significantly when appreciably different fields in distinct point of the workspace are requested (such as during independent control). Consequently, a magnetic setup capable of generating such fields and gradients, without incurring in magnetic saturation or overheating, is required.

TABLE I
DESIGN REQUIREMENTS

Requirement	Motivation
No electromagnetic force when the setup is off	Safety in case of system failure
Control of two robots with three Degrees Of Freedom (DOF) each	To enhance the complexity of performable tasks
Workspace size of at least $30\times30\times30$ mm^3 with accessibility of a sphere of 50 mm diameter	This volume would be enough to perform *ex-vivo* and *in-vivo* experiments on laboratory mice
No singularities in the workspace during control in 3D-space	Singularities would compromise the stability of the system and cause undesired behaviour
The system should levitate a 1 mm microrobot in liquid without reaching temperatures above 80°C	Ensure a margin of possible overload before overheating the electromagnets (120°C)

Note: We define workspace accessibility as the largest object with convex volume that can be centered in the experimental setup without interference.

For reasons of control and safety, these strong fields are commonly generated using electromagnetic coils. As effective as electromagnets may be, they require high currents for such actuation. In turn, high currents result in significant Joule heating, compromising performance, and, possibly, even stability. For these reasons, efficient techniques for current minimization and thermal management of the coils are fundamental for the safe operation of microrobots.

In this study, we present and experimentally validate a newly designed system capable of independently controlling identical and nonidentical microrobots in the 3-D-space. This is achieved by exploiting the inhomogeneity of the strong fields the system can generate. Moreover, we present a thermal management solution to prevent the overheating of the electromagnetic coils. Finally, the performance of the overall setup is experimentally evaluated during independent six-DOF control. The significant contributions of the paper can be summarized as follows:

1) Analysis, design, and assembly of a electromagnetic setup for the independent control of (identical and nonidentical) robots in the 3-D-space (see Section II).
2) Design and analysis of a thermal management strategy for the electromagnets (see Section II-B).
3) Modeling and singularity analysis of the electromagnetic setup and of the used microrobots (see Section III-B, Appendix B).
4) Development of a control strategy and 3-D-space state-reconstruction procedures for independentsix-DOF control of microrobots (see Section III-A).
5) Development and comparison of several techniques for force-to-current mapping with minimal current request (see Section III-D).

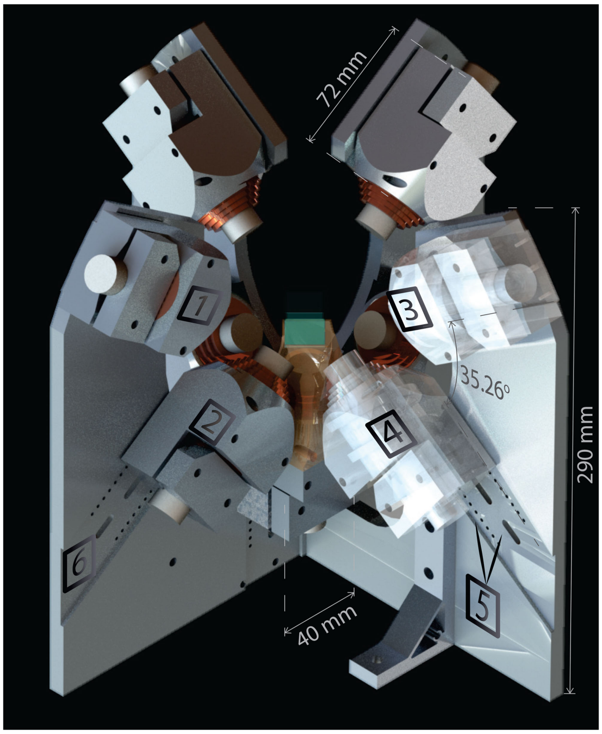

Fig. 2. Computer assisted rendering showing the variable workspace accessibility of the setup. Coils $\boxed{1}$ and $\boxed{3}$ are set to maximum distance to offer increased accessibility (*workspace accessibility:* a sphere of diameter 160 mm). Coils $\boxed{2}$ and $\boxed{4}$ are set at minimum distance which offer the strongest operational fields (*workspace accessibility:* a sphere of diameter 50 mm). The coils can move in steps of 5 mm, and are fixed to the frame using the holes and slots shown in $\boxed{5}$. Finally, a rectangular groove $\boxed{6}$ ensures precise alignment. For improved clarity coils, $\boxed{3}$ and $\boxed{4}$ are rendered using a transparency option. The overall setup can be enclosed in a $300 \times 300 \times 290$ mm^3 cuboid.

6) Experimental independent six-DOF control of two identical and nonidentical microspheres (see Section IV).

II. Hardware Design

This section presents the key design points that allowed the setup to perform independent control of two microrobots in the 3-D-space. The design process aims at satisfying a set of minimal requirements. These are listed and discussed in Table I. The final testbed is shown in Figs. 1 and 2.

A. Design Choices and Final Design

Guided by the requirements provided in Table I, several designs are developed and evaluated using finite element (FE) analysis software (COMSOL Multiphysics, COMSOL Inc., Stockholm, Sweden). Safety requirements lead us to choose electromagnetic coils over permanent magnets, as the former are inert when shut down in case of emergency. The power requirements for actuation of paramagnetic microscopic robots using air-core electromagnets render them unusable from a thermal point of view. Therefore, Vacoflux-core coils are used in the setup.

Further, it should be noted that not only does the control of multiple microrobots require strong magnetic fields and magnetic field gradients (for magnetization and force exertion), but it also requires swift spatial changes of the magnetic force, and hence of the magnetic gradient. At a given position ($\mathbf{p} \in \mathbb{R}^3$), this change is represented by the third-order tensor ($\mathbf{E}(\mathbf{p}) \in \mathbb{R}^{3\times3\times3}$) collecting the Hessian matrices of each component of the field. However, due to the quantized nature of FE, we found the estimation of $\mathbf{E}$ to be unreliable. Furthermore, it is challenging to correlate the independent control requirements to optimal values of each element of $\mathbf{E}$.

TABLE II
Specifications of the Final Coil Design

Parameter	Value
Wire Diameter	0.6 mm
Number of Turns	1274
Maximum Coil Length	50 mm
Coil Inner Diameter	20 mm
Coil Outer Diameter	41 mm
Resistance (20 °C)	8.4 Ω
Core Diameter	20 mm
Core Length	100 mm

Alternatively, we first design a specimen electromagnet that respects the requirements in Table I. Successively, we maximize the field and gradient output of such electromagnetic coil (see Fig. 3), as these values are in scalar relation with the Hessian values. In order to address the higher order inverse dependence of the Hessian terms on the distance, the considered values are corrected dividing them by the distance from the coil (gradients) and its square (field). Finally, the arrangement of the coils is fixed to spherical, to guarantee the accessibility requirement, and an optimization routine (MATLAB, Mathworks, Natick, USA) is used to determine the optimal position and number of coils. This optimization aims at minimizing total power consumption during the exertion of 7800 pairs of forces with varying intensity, direction, and exertion points. Three constraints are enforced in this optimization routine: the maximum and minimum current to avoid saturation, the minimum distance (in polar coordinates) between electromagnets (to avoid overlapping), and the minimum distance between electromagnets and cameras (which are assumed to be positioned on two planar sides, as in the current setup, as well as on top). It is worth noting how the high-order dependence of $\mathbf{E}$ on the distance from the coils, leads to better multiagent performance with systems with closely grouped electromagnets. This distance sensitivity is decreased in systems designed for force-controlled steering, and even further reduced in system for torque-based control only.

The final design (BatMag) consists of nine electromagnetic coils positioned as shown in Figs. 1 and 2. The parameters of these metal-core electromagnets are presented in Table II. Additionally, Fig. 2 shows how the requirements on workspace size and accessibility have been addressed. All actuators, including the electromagnets, are controlled using third-party servo drives (Elmo Motion Control, Petach-Tikva, Israel). In the workspace center, BatMag is capable of generating magnetic fields and gradients of upto 160 mT and 3.6 T/m, respectively, for the configuration used in the presented experiments (see Table III).

B. Thermal Management

Hitherto, only a few studies discuss and quantitatively analyze the thermal management of electromagnetic coils. Yet, this is a crucial aspect for the reliable operation of such

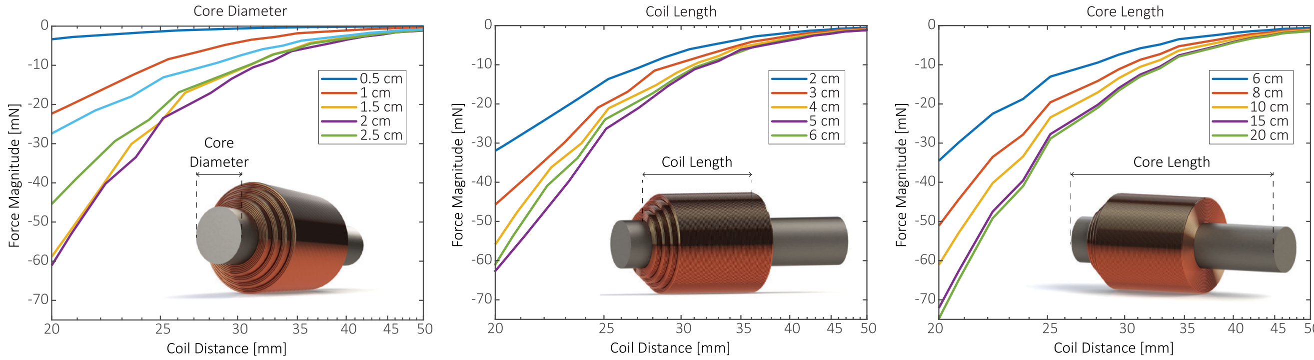

(a) (b) (c)

Fig. 3. Plots depicting the theoretical electromagnetic force exerted by a single coil on a paramagnetic dipole positioned along the coil's axis. The distance value represents the normal distance from the metal core, while the paramagnetic dipole has unitary magnetic constant (k_{mag}) (10). A single parameter is varied throughout the simulation, while the other ones are consistent with Table II. The power input of the simulated coil is set 40 W. (a) Effects of core size are depicted. For accessibility requirements the maximum diameter of the coil is set to 41 mm. Thus, in this plot the thickness of the coil—and consequently the number of turns—decreases as the core diameter increases. (b) Force dependency on the length of the coil is represented. Also, here a tradeoff is present. In point of fact, a longer coil—at equal current—exerts a stronger magnetic field. Yet, this comes at the cost of a longer copper wire and, therefore, higher resistance and lower current for equal power input. (c) Electromagnetic force with respect to the length of the electromagnetic core; the distance between the core and the center of the workspace is maintained constant. Here, a longer core shows (incrementally smaller) force increases over shorter ones. However, the increase in field comes with an increased mass, which requires an oversized frame, and a decrease in the bandwidth of the electromagnet due to the increase in the magnetic energy stored in it.

TABLE III
COMPARISON OF BATMAG WITH SEVERAL EXISTING ELECTROMAGNETIC SETUPS FOR MICROROBOTICS

Setup [reference]	BatMag	Octomag [24]	Rahmer *et al.* [5]	Diller *et al.* [25]	MobiMag [26]	Niu *et al.* [23]
Workspace	$35\times35\times35$ mm^3	⌀25 mm semi-sphere	⌀20 cm sphere	$20\times20\times20$ mm^3	18×18 mm^2	⌀20 mm sphere
Maximum Workspace Accessibility	⌀160 mm sphere [⌀60 mm as reported]	⌀130 mm semi-sphere	cylinder of over ⌀$20\times\infty$ cm^3	$120\times120\times120$ mm^3	40×40 mm^2	⌀110 mm sphere
Maximum field flux at the center (mT)	160	15	400 vertical 100 horizontal	15	15	40
Maximum gradient at the center (mT/m)	3575	200	3000	100	60	250
Number of electro-magnets	9	8	18	8	4	6

Note: BatMag shows improvements of up to an order of magnitude in the intensity of the generated electromagnetic field and gradient. Furthermore, fields are achieved in a workspace volume of up to five times larger than previous literature The fields and gradients of BatMag are reported with the configuration used to perform the presented experiments, offering a workspace accessibility of a⌀60 mm sphere. *Data reproduced from [23].*

electromagnets. In point of fact, during operation a single electromagnetic coil can reach a power of consumption of 450 W. Only a very limited amount of this power is converted in kinetic/potential energy of the controlled microrobots. Part of the transformed energy goes into generating the electromagnetic field and magnetizing the electromagnetic core (see Appendix A). However, at steady state, the majority of the provided energy is dissipated in the form of Joule losses. Due to the low heat capacity of copper (0.385 J/g°C) and to the limited (external) surface/volume ratio of the coils, the electromagnets—if not cooled—can reach extreme temperatures, posing a risk to the users and the overall electrical system.

Therefore, guided by the FE model, we design a water cooling system to transport the heat from the coils to an aluminum radiator (see Fig. 4). Silicone hoses are clamped against the coils for this purpose. Additionally, the frame is designed in aluminum (205 W/m· K) to act as passive heat-sink. Water-cooling is preferred over oil-cooling for its superior performance and increased ease of sterilization in clinically relevant applications.

The nondissipated heat increases the temperature of the coils and, consequently, their resistance. This increase can be estimated using the linear approximation of the steady-state resistivity dependence on temperature

$$R(T) = R_0[1 + \alpha(T - T0)] \tag{1}$$

where $T \in \mathbb{R}$ is the temperature of the coil, $R_0 \in \mathbb{R}$ (8.4 Ω) is the resistance of the coil at room temperature $T_0 \in \mathbb{R}$ (23.7 $\pm$ 0.1 °C), and $\alpha \in \mathbb{R}$ the temperature coefficient of resistivity (0.0039 °C^{-1} for copper). Substituting (1) in Ohm's law ($V = RI$), we obtain

$$T = \frac{V - IR_0}{IR_0\alpha} + T_0 \tag{2}$$

where I is the applied current and V the measured voltage. Consequently, substituting in (2), the voltage and current output of the power supplier, we are able to indirectly measure the temperature of the coil during operation at several continuous currents—which correspond to root mean square (RMS) ratings in noncontinuous operation. In particular, these experimentally

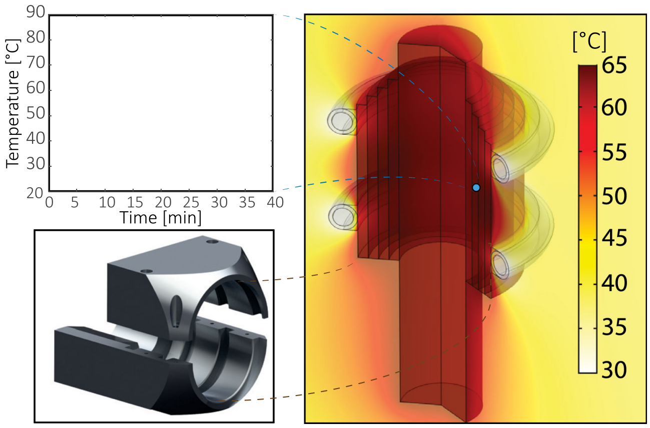

Fig. 4. *Right:* Section showing the temperature, according to finite element (FE) analysis, of the cooled electromagnetic coil at steady state when provided a continuous current of 2 A. The lower temperature of the experimental results is due to the unmodeled convective effects and heat-sinking capabilities of the aluminum clamp and frame, which have been neglected to ensure conservative results. *Top-left:* Time-dependency of the highest temperature in the electromagnetic coil when provided a current of 2 A (data from FE model). *Bottom-left:* Exploded rendering of the clamp used to position the cooling hose on the electromagnetic coil. Efficient heat exchange is ensured by the presence of thermoconductive paste (8 W/m· K) along the contact area of the clamp with the coil and cooling hose.

estimated temperatures at steady state are 36 ± 3 °C, 53 ± 3 °C, and 82 ± 3 °C for current values of 1.5 A, 2 A, and 2.5 A, respectively. The heating process takes about 12min to reach 63.2% of its final value. Conversely, after powering down the coils, the cooling system is able to reduce their temperature from 84 to 30 °C in 7:30 min. Remarkably, at just 1.5 A current rating, without cooling, the electromagnet has an experimentally estimated steady-state temperature of 125 ± 3 °C (5 °C above the insulation safety limit), while at 2 A the coil reaches 117 ± 3 °C in 12 min, hence compromising further continuous operation at this rating.

A maximum of about 1.5 A per coil is required to levitate a 1 mm iron sphere. Therefore, also the requirements regarding heat-dissipation are considered satisfied. Furthermore, throughout the experiments, we present (see Section IV) the coils never reached the safety limit of 120 °C.

III. Software Implementation

This section presents the software infrastructure, we developed to perform independent six-DOF control of microrobots. The custom software receives the position and desired trajectory, and outputs the currents at the electromagnets required for actuation (see Fig. 5).

A. Camera Calibration and Tracking

For imaging and tracking purposes, two Grasshopper three cameras (FLIR, Wilsonville, USA) are attached to an equal number of orthogonally oriented zoom modules with adjustable magnification (Qioptiq, St Asaph, U.K.). Using this imaging setup, we develop an algorithm capable of tracking the microrobots in a time window suitable for the control frequency (20 ms for the processing of both the images of size 2028 × 2048 pixels each). The simple—yet effective—technique, we used is depicted in Fig. 5. The procedure outputs two points on the two cameras image plane. A linear triangulation of the two points is then performed [27]. This results in the 3-D-space coordinates of the tracked microdevice.

B. Modeling and Control

The obtained position can then be used in the developed model. In particular, the motion of a magnetic microrobot can be modeled according to

$$\mathbf{F}_{em} + \mathbf{F}_d + \mathbf{F}_i + \mathbf{F}_g + \mathbf{F}_b = 0 \tag{3}$$

$$\mathbf{I}\alpha + \mathbf{T}_{em} + \mathbf{T}_d = 0 \tag{4}$$

where $\mathbf{F}_{em} \in \mathbb{R}^3$ are the electromagnetic forces, $\mathbf{F}_d \in \mathbb{R}^3$ are the drag forces, $\mathbf{F}_g \in \mathbb{R}^3$ are the gravitational forces, $\mathbf{F}_i \in \mathbb{R}^3$ are the other inertial forces, $\mathbf{F}_b \in \mathbb{R}^3$ are the buoyancy forces, $\mathbf{I} \in \mathbb{R}^{3\times3}$ is the moment of inertia, $\alpha \in \mathbb{R}^3$ is the angular acceleration, $\mathbf{T}_{em} \in \mathbb{R}^3$ is the electromagnetic torque, and $\mathbf{T}_d \in \mathbb{R}^3$ is the rotational drag.

In this study, the microrobot move in silicon oil with dynamic viscosity of 0.001 m^2/s. Therefore, for submillimeter velocities, their Reynolds number will not be above 0.01 [28]. In this low-Reynolds number environment, the forces acting on the microrobots (3) are as follows:

$$\mathbf{F}_i = M\mathbf{a} \tag{5}$$

$$\mathbf{F}_g = M\mathbf{g} \tag{6}$$

$$\mathbf{F}_b = -\mathbf{g}V\rho_m \tag{7}$$

$$\mathbf{F}_d = -\frac{1}{2}\rho_m C_D A\mathbf{v} \tag{8}$$

$$\mathbf{F}_{em} = \nabla(\mathbf{B}\cdot\mathbf{m}) \tag{9}$$

where $\mathbf{a} \in \mathbb{R}^3$ is the acceleration of the structure and $M \in \mathbb{R}$ is its mass, $\mathbf{g} \in \mathbb{R}^3$ is the gravitational acceleration, $V_s \in \mathbb{R}$ is the volume of the microrobot, and $\rho_m \in \mathbb{R}$ is the density of medium that surrounds it (970 kg/m^3). Further, $\mathbf{v} \in \mathbb{R}^3$ is the speed of the microrobot relative to the fluid, $A \in \mathbb{R}$ is its cross sectional area, $C_D \in \mathbb{R}$ is the drag coefficient (0.5 for our microrobots [29]). Finally, $\mathbf{m} \in \mathbb{R}^3$ is the magnetic dipole moment of the microrobot.

The microrobots used in this study are submillimeter microspheres. Being constructed of soft magnetic material, the remnant magnetization of the microsphere is negligible when compared to the magnetization due to the external magnetic field. This, combined with the extremely low time response of magnetization [30], [31], results in

$$\mathbf{m} = \iiint_V \mathbf{M}\,dV = \frac{4}{3}\pi r^3\left(\mathbf{M}_r + \frac{\chi}{\mu_0(1+\frac{\chi}{3})}\mathbf{B}_i\right) \approx \approx k_{\text{mag}}\mathbf{B}_s \tag{10}$$

where $r \in \mathbb{R}$ is the radius of the sphere, $\mathbf{B}_s \in \mathbb{R}^3$ is the magnetic field density at the surface of the sphere (assumed to be constant), and $\mathbf{B}_i = \frac{2}{3}\mathbf{B}_s$ is the magnetic field density inside the sphere—reduced by the demagnetizing H-field inside the microsphere [32]. Moreover, $\mathbf{M}_r \in \mathbb{R}^3$ is the remnant magne-

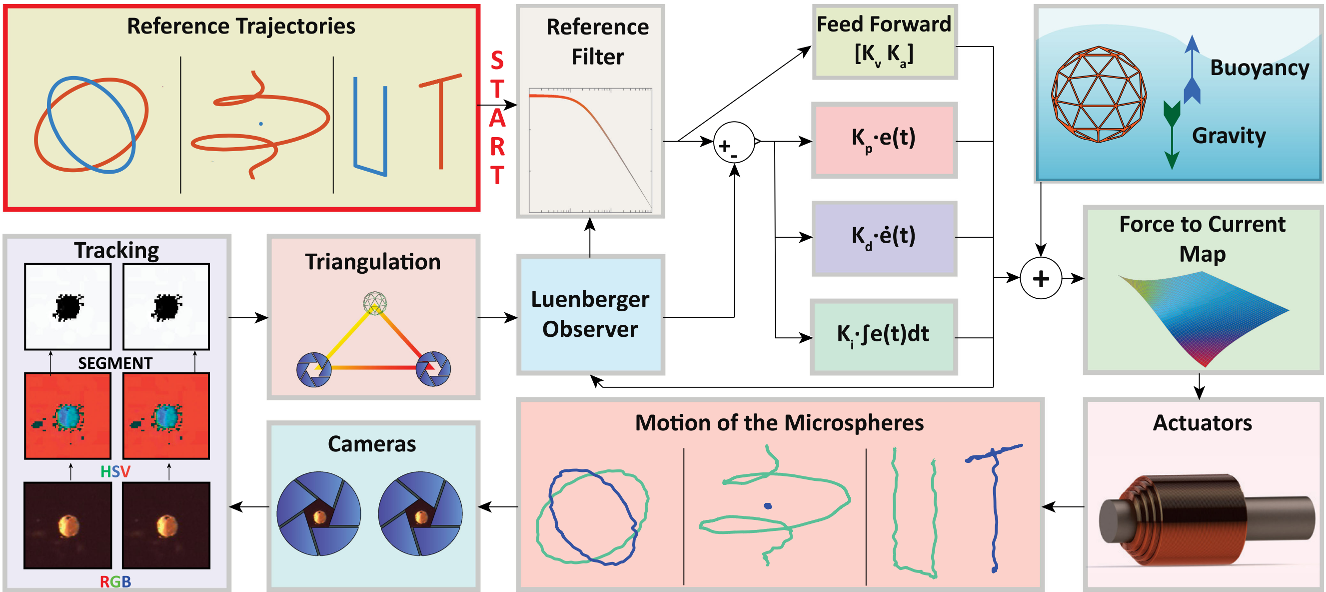

Fig. 5. Flowchart depicting the software structure of the developed setup. For tracking purposes, the cameras image the motion of the microspheres. These images are converted to hue-saturation-value (HSV) colorspace for better contrast among channels. During the tracking procedure, the HSV image is then thresholded using experimentally determined values, and the center of the largest blob is selected as the position of the microsphere in the camera. Finally, the two camera positions are triangulated as described in Section III-A. The variable [e(t)] represents the error between the observed position and the prescribed reference. K$_p$, K$_i$, and K$_d$ are the feedback proportional, integral, and derivative gains, respectively; K$_v$, and K$_a$ are the feedforward gains on velocity and acceleration, respectively.

tization (negligible for soft magnetic materials), $\mu_0 \in \mathbb{R}$ is the magnetic permeability of vacuum, and $\chi \in \mathbb{R}$ is the magnetic susceptibility of the sphere. For notational simplicity, the quantity $\pi r^3 \frac{8\chi}{3\mu_0(3+\chi)}$ will be denoted k_{mag}. Finally, for reasons of symmetry, the orientation and torques of the microsphere can be neglected.

Based on the presented model (4), a multiple-input multiple-output position PID with velocity and acceleration feedforward is developed for six-DOF motion control (see Fig. 5). Velocity and position are estimated using a Luenberger observer [33]. The references are preset according to the desired trajectory, and provided to the control loop as waypoints. These waypoints are preprocessed by a filter with four coincident poles to provide continuous derivatives to the controller. The time constant of such filter is proportional to the (observed) distance between the microrobot and the waypoint. The controller output the desired electromagnetic forces acting on the microrobots.

C. Force to Current Map

In order to reach actuation, the computed forces need to be mapped into currents at the electromagnets. The first step of this process is to develop a model of the field generated by the electromagnets. Consequently, we validate the FE results using a calibrated three-axis teslameter (Senis AG, Zug, Switzerland). The validation is performed along a grid of $10 \times 10 \times 10$ points spaced through the $35 \times 35 \times 35$ mm^3 workspace. In line with previous literature, we find the measured and simulated field values to be congruous with the exception of a scaling factor [24], [26].

The corrected FE data is then used to compute the function ($\widetilde{\mathbf{B}} \in \mathbb{R}^{3\times 9}$) mapping the currents at the electromagnets to the electromagnetic field ($\mathbf{B} \in \mathbb{R}^3$) in the workspace. A polynomial function was used for this purpose and computed using a least square minimization algorithm with an empirical weight to minimize the changes in convexity of the mapping function. Further, the said function is constrained to have null divergence and curl, according to Maxwell's equations. Finally, the order of the polynomial function was empirically chosen as five, as it offered the lowest errors while still preserving limited higher-order derivatives. This function allows us to map currents into fields at a given position in the workspace. Furthermore, computing the gradient of this function, we are able to map currents into magnetic gradients in the workspace and verify the presence of possible singularities (see Appendix B).

If we substitute (10) in (9), we can see that the force exerted on a microrobot is

$$\begin{aligned}\mathbf{F}_{em}(\mathbf{I}) &= \nabla(\mathbf{B}(\mathbf{I}) \cdot \mathbf{m}(\mathbf{I})) = \nabla\left(\mathbf{B}(\mathbf{I})^T k_{\text{mag}} \mathbf{B}(\mathbf{I})\right)\\ &= k_{\text{mag}} \nabla\left(\mathbf{I}^T \widetilde{\mathbf{B}}^T \widetilde{\mathbf{B}} \mathbf{I}\right).\end{aligned} \tag{11}$$

This set of equations has to be inverted to obtain the force-to-current map, required for the conversion of the control output. Yet, the nonlinearity—with respect to both position and currents—and nonconvexity (see Appendix C) of these functions renders it particularly arduous to find an analytic solution to this problem.

D. Numerical Solution

Alternatively, we investigate two numerical approaches to obtain the force-to-current map, which are as follows.

1) Nonlinear Optimization: The first approach uses the interior-point method (IPM) to solve a nonconvex quadratically constrained quadratic optimization [35]:

Input: $\mathbf{p}_j \in \mathbb{R}^3$, $\mathbf{F}_j \in \mathbb{R}^3$; for $j \in \{1, 2\}$
Result: $\mathbf{I} \in \mathbb{R}^9$
Objective function:
$\min \mathbf{I}^T \mathbf{I}$
subject to:
$\mathbf{F}_j = k_{\text{mag, j}} \nabla(\mathbf{I}^T \widetilde{\mathbf{B}}(\mathbf{p_j})^T \widetilde{\mathbf{B}}(\mathbf{p_j})\mathbf{I})$
$\mathbf{I} < \mathbf{I}_{\max}$
$\mathbf{I} > -\mathbf{I}_{\max}$
end

where $\mathbf{I} \in \mathbb{R}^9$ is the current at the electromagnets, $\mathbf{I}_{\max} \in \mathbb{R}^9$ is the maximum current at the electromagnets, $k_{\text{mag, j}} \in \mathbb{R}$ is the magnetic constant of the *j*-th microrobot, $\mathbf{p}_j \in \mathbb{R}^3$ is its position, $\mathbf{F}_j \in \mathbb{R}^3$ is the desired force, and $\widetilde{\mathbf{B}}(\mathbf{p_j}) \in \mathbb{R}^{3\times 9}$ is the position-dependent matrix mapping the currents to the electromagnetic field.

2) Semidefinite Approximation (SDA): The second approach aims at solving the following SDA with nuclear norm minimization (SDANM) of the problem:

Input: $\mathbf{p}_j \in \mathbb{R}^3$, $\mathbf{F}_j \in \mathbb{R}^3$; for $j \in \{1, 2\}$
Result: $\mathbf{J} \in \mathbb{S}^9$
Objective function:
$\min_{\mathbb{S}^9} \operatorname{tr}(\mathbf{J}) + w||\mathbf{J}||_*$
subject to:
$F_{i,j} = 2k_{\text{mag}} \operatorname{tr}[\widetilde{\mathbf{B}}(\mathbf{p_j})^T \widehat{\mathbf{B}}_i(\mathbf{p_j})\mathbf{J}]$
$\mathbf{J} \geq 0$
end

for $i \in \{x, y, z\}$, where

$$\widehat{\mathbf{B}}_i(\mathbf{p_j}) = \frac{\partial}{\partial \mathbf{p_j}_i} \widetilde{\mathbf{B}}(\mathbf{p_j}) \tag{12}$$

where $\mathbf{p_j}_i \in \mathbb{R}$ is the ith component of the position of the jth microrobot, and $F_{i,j} \in \mathbb{R}$ is the ith component of the force on the jth microrobot. Further, $\mathbf{J} = \mathbf{I}\mathbf{I}^T$, $\operatorname{tr}(\cdot)$ indicates the trace operator, $||\mathbf{J}||_*$ is the nuclear norm of $\mathbf{J}$, $w \in \mathbb{R}$ is an empirically determined weight, and $\mathbb{S}^9$ is the set of all 9×9 real-symmetric matrices. Additionally, $\mathbf{J} \geq 0$ indicates $\mathbf{J}$ has to be positive semidefinite. Finally, $\mathbf{I}$ is extracted as the eigenvector associated with the largest eigenvalue.

This optimization drops the nonconvex constraint of $\operatorname{rank}(\mathbf{J}) = 1$. However, a convex relaxation of the rank minimization is introduced adding a weighted term for the minimization of the nuclear norm of $\mathbf{J}$ in the cost function [36]. Moreover, in order to address for electromagnetic saturation, if the resulting solution exceeds the currents limits it is scaled according to

$$\mathbf{I}^* = \frac{\mathbf{I}}{\alpha}, \qquad \text{where} \qquad \alpha = \max_k \frac{|I_k|}{I_{\text{max,k}}} \tag{13}$$

for $k \in \{1, \ldots, 9\}$, where $\mathbf{I}^* \in \mathbb{R}^9$ is the scaled solution, I_k and $I_{\text{max,k}}$ are the kth elements of $\mathbf{I}$ and $\mathbf{I}_{\max}$, respectively. The scaling in (13) maintains the direction of the force while decreasing its magnitude below saturation.

2) Discussion: The performance of the optimizations are compared on the same 1000 random combinations of points and forces in the workspace. All combinations are selected to have solutions below $\mathbf{I}_{\max}$. Additionally, for comparison purposes, also the SDA proposed in [22] is implemented.

TABLE IV
PERFORMANCE COMPARISON OF THE OPTIMIZATION TECHNIQUES

	Rel. Error	Max. Rel. Error	Runtime *(ms)*
IPM	$(13.54\pm2.72)\times10^{-8}$	7.98×10^{-6}	63 ± 0.14
SDA	0.19 ± 0.24	1.88	670 ± 210
SDANM	0.095 ± 0.2	1	780 ± 370

Note: Average and maximum relative error (rel. error and max. rel. error, respectively) are reported as the relative error of the Euclidean norm. The abbreviations are as follows: IPM (interior point method), SDA (semidefinite approximation), and SDANM (semidefinite approximation with nuclear norm). The higher runtime of SDA and SDANM is likely due to the higher number of variables in these implementations (45, instead of 9 for IPM). The higher error is likely due to the convex-relaxations of these routines. All techniques are implemented in MATLAB on a UBUNTU-based computer (Xeon E3@3.50 GHx $\times$ 8, Quadro K2200 and 16 GB RAM). Further, CVX is used for the modeling of the semidefinite approximations [34].

As shown by the results (see Table IV) IPM outperformed the SDA (both with and without the nuclear norm term) in terms of average run-time, as well as average and maximum error; therefore, it is used in our experiments. Nonetheless, the hereby presented SDANM offers the state-of-the-art alternative among algorithms with polynomial complexity. This renders it preferable for implementation in hard real-time systems or environments with a high number of controlled variables. Finally, it should be noted that the average runtimes are reduced of about an order of magnitude when computing continuous trajectories in which the previous current is provided as initial solution of the optimization routine.

Particularly, in this study, the average IPM runtime is 7 ms, and its execution time is bound to a maximum of 20 ms. This would results in peak control frequencies of above 40 Hz. However, to ensure a constant bandwidth, the six-DOF control loop is constrained at 25 Hz. The software executes on a computer running Robot Operating System "Lunar Loggerhead" [37].

IV. Experimental Evaluation

In order to validate the novel design and techniques, we perform three experiments using both identical and nonidentical microspheres. In all the experiments, the magnetic microspheres are submerged in silicone oil, inside a $22 \times 22 \times 22$ mm^3 cube of hydrolytic class one borosilicate glass (170 μm thick) (see Fig. 1). *Please, refer to the accompanying video for the visualization of characteristic examples of the following experiments. Please, also note that errors are reported in the form Root Mean Square $\pm$ Standard Deviation (RMS $\pm$ SD).*

In the first experiment, two microspheres with radii of 350 μm move along two great circles, sections of an imaginary sphere (see Fig. 6). This imaginary sphere has a radius of 3 mm and is concentric with the workspace. The two paths are chosen on planes perpendicular both to each other, and to the optical axes of the cameras. In the five performed trials, the microrobots are able navigate the prescribed trajectory with error and average velocities of 97 $\pm$ 47 μm and 209 μm/s, respectively.

In the second experiment, two microspheres with radii of 350 μm are used. The first microsphere is maintained still in the center of the workspace, while the second microrobot inscribes it in a vortex-like trajectory (see Fig. 6). In the five performed

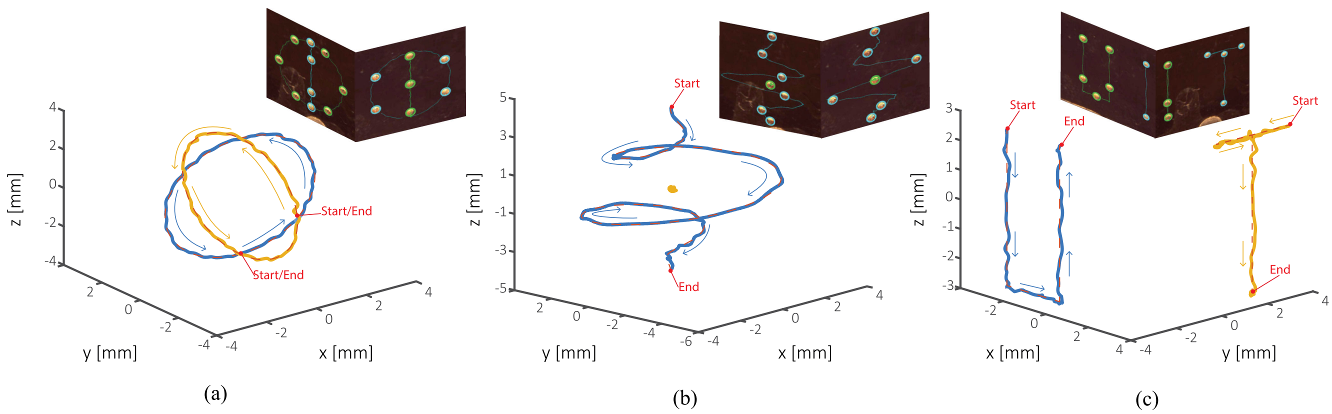

Fig. 6. Figure depicts representative trajectories for the independent control experiment. The dashed lines represent the prescribed trajectory, the solid lines show the path followed by the microspheres. Timelapses of the experiments are shown on top of the respective trajectory. (a) Two microspheres (radius 350 μm) are moving along two perpendicular great circles on a sphere of radius 3 mm. (b) Microsphere (radius 350 μm) moving along a vortex-like path around a second, equally sized, microsphere levitating at the center of the workspace. (c) Two nonidentical microspheres—with radii of 350 and 250 μm—simultaneously tracing the letters *U* and *T*, respectively. *Please, refer to the accompanying video for the visualization of characteristic examples of these experiments.*

trials, we find the still microrobot to maintain its prescribed position with an average error of 82 ± 40 μm, while the moving one performs its trajectory with error and average velocity of 77 ± 32 μm and 122 μm/s, respectively.

In the third experiment, we demonstrate the capability of the system to manipulate nonidentical microrobots. Consequently, we use two microspheres of different radii (250 and 350 μm) to trace *U*-shaped and *T*-shaped trajectories (see Fig. 6). Sinusoidal velocities are used as reference along the straight segments in the trajectory. Three trials are performed, in which the error and average velocities of the microrobots are found to be, respectively, 71 ± 41 μm and 171 μm/s—for the 250 μm microsphere—and 112 ± 52 μm and 208 μm/s—for the 350 μm microsphere.

Finally, it is worth noticing that despite the theoretically perfect isotropy of the microsphere—that should result in its almost immediate remagnetization, with no consequent electromagnetic torque exertion—some rare, but sudden, rotation are observed. We hypothesize that these are due to crystal anisotropy, to physical inhomogeneity and to the drag acting on the dye of the microsphere. Yet, these rotations did not seem to affect the motion, as positioning error remained in line with the rest of the trial.

V. Conclusion

In this study, we design, simulate, develop, and experimentally validate an electromagnetic setup for independent 3-D control of microrobots. Throughout the design process, we determine the most relevant parameters for the generation of strong electromagnetic fields, and for the dissipation of the generated heat. Exploiting this analysis, we build a setup capable of generating magnetic fields and gradients of, respectively, 160 mT and 3.6 T/m. These values are made more notable by their combination with a workspace of $35 \times 35 \times 35$ mm^3, with maximum workspace accessibility of 160 mm. Moreover, a thermal management technique is developed and quantitatively analyzed to prevent overheating during continuous operation. Furthermore, two novel techniques—with deterministic and NP complexities—for force-to-current mapping are presented and evaluated. The performance of such setup is not only tested and evaluated for the six-DOF independent navigation of identical microrobots (with peak velocities of 0.4 body-lengths/s), but also for the independent six-DOF control of nonidentical ones (with RMS errors lower than 0.15 body-lengths). The demonstrated capabilities suggest that these techniques might be used for precise collaborative tasks in the microscopic world, with potential applications in fields such as minimally invasive surgery, microassembly, micromanipulation, tissue engineering, and lab-on-a-chip applications.

Future work will investigate the use of these techniques for tasks of micromanipulation and microassembly. Further, control algorithms regulating more DOF and aimed at current-minimization will be studied. Moreover, more efficient tracking algorithms, possibly exploiting the epipolar nature of the cameras, will be investigated. Finally, we will study the development of similar techniques for the control of swarms, as well as the use of clinically compatible imaging systems (such as ultrasound [38]).

Appendix A
Energy Stored in the Magnetic Field and Electromsagnetic Core

The following amount of energy is necessary for generating the electromagnetic field (W_F) and magnetizing the electromagnetic core (W_M):

$$\mathrm{d}W_F = \iiint_{V_E} (\mathbf{H} \cdot \mathrm{d}\mathbf{B}) \mathrm{d}V_E \tag{14}$$

$$\mathrm{d}W_M = \mu_0 \iiint_{V_E} (\mathbf{H} \cdot \mathrm{d}\mathbf{M}) \mathrm{d}V_E. \tag{15}$$

where $\mathbf{H} \in \mathbb{R}^3$ and $\mathbf{B} \in \mathbb{R}^3$ are the magnetic H-field and the magnetic flux density, respectively, V_E is the volume surrounding the coil, $\mathbf{M} \in \mathbb{R}^3$ is the magnetization, and $\mu_0 \in \mathbb{R}$ is the magnetic permeability of vacuum.

Appendix B
Singularity Analysis of the Actuation System

To identify the possible singularities in our actuation system, we analyze the Jacobian ($\mathbf{J} \in \mathbb{R}^{6\times 9}$) of the electromagnetic force with respect to the current

$$\mathbf{J} = \begin{bmatrix} \frac{\delta}{\delta I_1} F^x_{em,1}(\mathbf{p_1}) & \cdots & \frac{\delta}{\delta I_9} F^x_{em,1}(\mathbf{p_1}) \\ \frac{\delta}{\delta I_1} F^y_{em,1}(\mathbf{p_1}) & \cdots & \frac{\delta}{\delta I_9} F^y_{em,1}(\mathbf{p_1}) \\ \frac{\delta}{\delta I_1} F^z_{em,1}(\mathbf{p_1}) & \cdots & \frac{\delta}{\delta I_9} F^z_{em,1}(\mathbf{p_1}) \\ \frac{\delta}{\delta I_1} F^x_{em,2}(\mathbf{p_2}) & \cdots & \frac{\delta}{\delta I_9} F^x_{em,2}(\mathbf{p_2}) \\ \frac{\delta}{\delta I_1} F^y_{em,2}(\mathbf{p_2}) & \cdots & \frac{\delta}{\delta I_9} F^y_{em,2}(\mathbf{p_2}) \\ \frac{\delta}{\delta I_1} F^z_{em,2}(\mathbf{p_2}) & \cdots & \frac{\delta}{\delta I_9} F^z_{em,2}(\mathbf{p_2}) \end{bmatrix} \tag{16}$$

where $I_q \in \mathbb{R}^9$ is the current at the qth electromagnet and $F^i_{em,j}(\mathbf{p_j})$ is the i component of the electromagnetic force on the jth microrobot at position $\mathbf{p_j} \in \mathbb{R}^3$, with $i \in \{x, y, z\}$, $j = \{1, 2\}$, $q \in \{1, \ldots, 9\}$ and $\mathbf{p_1} \neq \mathbf{p_2}$.

The critical points of the system can be identified as the points in which $\mathbf{J}$ is rank deficient. At such critical points, the system loses DOF, compromising its independent actuation. These singularities might be due to the position of the microrobots, to the current at the electromagnets, or to a combination of the two.

In our case, we analytically find no current-independent critical point, meaning that no combination of positions of the microrobots alone affects the rank of $\mathbf{J}$. Yet, we found current dependent and current-and-position dependent critical points. These points correspond to singularities related to the physical expression of the electromagnetic force. Even though the resulting analytic solution is somewhat too intricate and extensive for intuitive understanding (due to the numerous coefficients of the polynomial function), the nature of these critical points becomes evident analyzing the following formulation of the electromagnetic force for $\mathbf{m} = k_{\text{mag}}\mathbf{B}$ [39]:

$$\mathbf{F} = k_{\text{mag}} \begin{bmatrix} \frac{\delta B_x}{\delta x} B_x + \frac{\delta B_x}{\delta y} B_y + \frac{\delta B_x}{\delta z} B_z \\ \frac{\delta B_x}{\delta y} B_x + \frac{\delta B_y}{\delta y} B_y + \frac{\delta B_y}{\delta z} B_z \\ \frac{\delta B_x}{\delta z} B_x + \frac{\delta B_y}{\delta z} B_y - \left(\frac{\delta B_x}{\delta x} + \frac{\delta B_y}{\delta y} \right) B_z \end{bmatrix}. \tag{17}$$

For instance, singularities can be noticed when the field in the considered point is zero (e.g., if all currents are zero) or when actuation along a component is not possible (e.g., if $\mathbf{m}$ is aligned with z but $\frac{\delta B_x}{\delta z} = 0$, then no force can be exerted along the *x*-axis).

Despite these singularities, we could not find any numerical set of positions and forces in the workspace, that only had solutions that rendered $\mathbf{J}$ rank deficient. Further, it should be noted that these singularities are intuitively avoided by the optimization in Section III, even when the respective inequalities are not included in the constraints of the optimization, as they would require infinite power for actuation.

Appendix C
Nonconvexity of the Quadratically Constrained Quadratic Optimization

Let us consider the general formulation of quadratically constrained quadratic programs:

Input: $\mathbf{Q}_0, \mathbf{Q}_i, \mathbf{Q}_l \in \mathbb{R}^{n\times n}, b_i, b_l \in \mathbb{R}, \mathbf{q}_0, \mathbf{q}_i, \mathbf{q}_l \in \mathbb{R}^n, \mathbf{l}, \mathbf{u} \in$
$\mathbb{R}^n; \mathcal{I} \cup \mathcal{E} = \{1, \ldots, m\}$
Output: $\mathbf{x} \in \mathbb{R}^n$
Objective function:
$\min \mathbf{x}^T \mathbf{Q}_0 \mathbf{x} + \mathbf{q}_0^T \mathbf{x}$
subject to:
$\mathbf{x}^T \mathbf{Q}_i \mathbf{x} + \mathbf{q}_i^T \mathbf{x} \leq b_i \quad i \in \mathcal{I}$
$\mathbf{x}^T \mathbf{Q}_l \mathbf{x} + \mathbf{q}_l^T \mathbf{x} = b_l \quad l \in \mathcal{E}$
$\mathbf{l} \leq \mathbf{x} \leq \mathbf{u}$.
end

In our case, $m = 3$ and $\mathbf{Q}_i = \frac{\delta}{\delta \mathbf{p}_i} \left(\widetilde{\mathbf{B}}(\mathbf{p})^T \widetilde{\mathbf{B}}(\mathbf{p}) \right)$ with p_i being the ith component of the position of the microrobot. This optimization problem is convex if and only if the matrices $\mathbf{Q}_0, \mathbf{Q}_i, \mathbf{Q}_l$ are all positive semidefinite or all negative semidefinite [40]. However, such matrices were experimentally found to be indefinite. Further, it should be noted that claiming that any $\mathbf{Q}$ is semidefinite would result in

$$\mathbf{x}^T \mathbf{Q} \mathbf{x} \geq 0, (\leq 0 \text{ for NSD}) \qquad \forall \mathbf{x} \neq \mathbf{0} \tag{18}$$

which would effectively constrain the direction of all forces.

References

[1] A. G. Banerjee, S. Chowdhury, S. K. Gupta, and W. Losert, "Survey on indirect optical manipulation of cells, nucleic acids, and motor proteins," *J. Biomed. Opt.*, vol. 16, no. 5, 2011, Art. no. 051302.

[2] S. Martel, "Magnetic navigation control of microagents in the vascular network: Challenges and strategies for endovascular magnetic navigation control of microscale drug delivery carriers," *IEEE Control Syst.*, vol. 33, no. 6, pp. 119–134, Dec. 2013.

[3] S. Chowdhury, W. Jing, and D. J. Cappelleri, "Controlling multiple microrobots: Recent progress and future challenges," *J. Micro-Bio Robot.*, vol. 10, no. 1–4, pp. 1–11, 2015.

[4] S. Lee *et al.*, "A capsule-type microrobot with pick-and-drop motion for targeted drug and cell delivery," *Adv. Healthcare Mater.*, vol. 7, 2018, Art. no. e1700985.

[5] J. Rahmer, C. Stehning, and B. Gleich, "Remote magnetic actuation using a clinical scale system," *PLoS One*, vol. 13, no. 3, 2018, Art. no. e0193546.

[6] A. Ghosh *et al.*, "Stimuli-responsive soft untethered grippers for drug delivery and robotic surgery," *Frontiers Mech. Eng.*, vol. 3, pp. 7–15, 2017.

[7] F. Ongaro, S. Scheggi, A. Ghosh, A. Denasi, D. H. Gracias, and S. Misra, "Design, characterization and control of thermally-responsive and magnetically-actuated micro-grippers at the air-water interface," *PLoS One*, vol. 12, no. 12, 2017, Art. no. e0187441.

[8] F. Guo *et al.*, "Three-dimensional manipulation of single cells using surface acoustic waves," *Proc. Nat. Acad. Sci.*, vol. 113, no. 6, pp. 1522–1527, 2016.

[9] A. G. Banerjee, S. Chowdhury, W. Losert, and S. K. Gupta, "Real-time path planning for coordinated transport of multiple particles using optical tweezers," *IEEE Trans. Automat. Sci. Eng.*, vol. 9, no. 4, pp. 669–678, Oct. 2012.

[10] Y. Wu, D. Sun, W. Huang, and N. Xi, "Dynamics analysis and motion planning for automated cell transportation with optical tweezers," *IEEE/ASME Trans. Mechatronics*, vol. 18, no. 2, pp. 706–713, Apr. 2013.

[11] S. Chowdhury *et al.*, "Automated cell transport in optical tweezers-assisted microfluidic chambers," *IEEE Trans. Automat. Sci. Eng.*, vol. 10, no. 4, pp. 980–989, Oct. 2013.

[12] M. V. Berry and A. K. Geim, "Of flying frogs and levitrons," *Eur. J. Phys.*, vol. 18, no. 4, 1997, Art. no. 307.

[13] S. Shahrokhi and A. T. Becker, "Stochastic swarm control with global inputs," in *Proc. IEEE/RSJ Int. Conf. Intell. Robots Syst.*, 2015, pp. 421–427.

[14] D. R. Frutiger, K. Vollmers, B. E. Kratochvil, and B. J. Nelson, "Small, fast, and under control: wireless resonant magnetic micro-agents," *Int. J. Robot. Res.*, vol. 29, no. 5, pp. 613–636, 2010.

[15] E. Diller, J. Giltinan, and M. Sitti, "Independent control of multiple magnetic microrobots in three dimensions," *Int. J. Robot. Res.*, vol. 32, no. 5, pp. 614–631, 2013.

[16] A. Becker, G. Habibi, J. Werfel, M. Rubenstein, and J. McLurkin, "Massive uniform manipulation: Controlling large populations of simple robots with a common input signal," in *Proc. IEEE/RSJ Int. Conf. Intell. Robots Syst.*, 2013, pp. 520–527.

[17] S. E. Chung, X. Dong, and M. Sitti, "Three-dimensional heterogeneous assembly of coded microgels using an untethered mobile microgripper," *Lab Chip*, vol. 15, no. 7, pp. 1667–1676, 2015.

[18] C. Pawashe, S. Floyd, and M. Sitti, "Multiple magnetic microrobot control using electrostatic anchoring," *Appl. Phys. Lett.*, vol. 94, no. 16, 2009, Art. no. 164108.

[19] D. Cappelleri, D. Efthymiou, A. Goswami, N. Vitoroulis, and M. Zavlanos, "Towards mobile microrobot swarms for additive micromanufacturing," *Int. J. Adv. Robot. Syst.*, vol. 11, no. 9, 2014, Art. no. 150.

[20] N. A. Torres and D. O. Popa, "Cooperative control of multiple untethered magnetic microrobots using a single magnetic field source," in *Proc. IEEE Int. Conf. Automat. Sci. Eng.*, 2015, pp. 1608–1613.

[21] D. Wong, E. B. Steager, and V. Kumar, "Independent control of identical magnetic robots in a plane," *IEEE Robot. Automat. Lett.*, vol. 1, no. 1, pp. 554–561, Jan. 2016.

[22] A. Denasi and S. Misra, "Independent and leader–follower control for two magnetic micro-agents," *IEEE Robot. Automat. Lett.*, vol. 3, no. 1, pp. 218–225, Jan. 2018.

[23] F. Niu, J. Li, W. Ma, J. Yang, and D. Sun, "Development of an enhanced electromagnetic actuation system with enlarged workspace," *IEEE/ASME Trans. Mechatronics*, vol. 22, no. 5, pp. 2265–2276, Oct. 2017.

[24] M. P. Kummer, J. J. Abbott, B. E. Kratochvil, R. Borer, A. Sengul, and B. J. Nelson, "OctoMag: An electromagnetic system for 5-DOF wireless micromanipulation," *IEEE Trans. Robot.*, vol. 26, no. 6, pp. 1006–1017, Dec. 2010.

[25] E. Diller, J. Giltinan, G. Z. Lum, Z. Ye, and M. Sitti, "Six-degree-of-freedom magnetic actuation for wireless microrobotics," *Int. J. Robot. Res.*, vol. 35, no. 1–3, pp. 114–128, 2016.

[26] F. Ongaro, C. Pacchierotti, C. Yoon, D. Prattichizzo, D. H. Gracias, and S. Misra, "Evaluation of an electromagnetic system with haptic feedback for control of untethered, soft grippers affected by disturbances," in *Proc. IEEE Int. Conf. Biomed. Robot. Biomechatronics*, 2016, pp. 900–905.

[27] R. I. Hartley and A. Zisserman, *Multiple View Geometry in Computer Vision*, 2nd ed. Cambridge, U.K.: Cambridge Univ. Press, ISBN: 0521540518, 2004.

[28] J. Happel and H. Brenner, *Low Reynolds Number Hydrodynamics: With Special Applications to Particulate Media*, vol. 1. Berlin, Germany: Springer, 2012.

[29] A. Bailey, "Sphere drag coefficient for subsonic speeds in continuum and free-molecule flows," *J. Fluid Mech.*, vol. 65, no. 2, pp. 401–410, 1974.

[30] M. Sharrock, "Particle-size effects on the switching behavior of uniaxial and multiaxial magnetic recording materials," *IEEE Trans. Magn.*, vol. 20, no. 5, pp. 754–756, Sep. 1984.

[31] B. Koopmans, J. Ruigrok, F. Dalla Longa, and W. De Jonge, "Unifying ultrafast magnetization dynamics," *Phys. Rev. Lett.*, vol. 95, no. 26, 2005, Art. no. 267207.

[32] B. D. Cullity and C. D. Graham, *Introduction to Magnetic Materials*. Hoboken, NJ, USA: Wiley, 2011.

[33] D. Luenberger, "An introduction to observers," *IEEE Trans. Autom. Control*, vol. 16, no. 6, pp. 596–602, Dec. 1971.

[34] M. Grant, S. Boyd, and Y. Ye, *CVX: MATLAB Software for Disciplined Convex Programming*. (2008). WordPress.

[35] W. H. Press, *Numerical Recipes 3rd Edition: The Art of Scientific Computing*. Cambridge, U.K.: Cambridge Univ. Press, 2007.

[36] B. Recht, M. Fazel, and P. A. Parrilo, "Guaranteed minimum-rank solutions of linear matrix equations via nuclear norm minimization," *SIAM Rev.*, vol. 52, no. 3, pp. 471–501, 2010.

[37] M. Quigley *et al.*, "ROS: An open-source robot operating system," in *Proc. ICRA Workshop Open Source Softw.*, Kobe, Japan, vol. 3, no. 3.2, pp. 5–10, 2009.

[38] S. Scheggi *et al.*, "Magnetic motion control and planning of untethered soft grippers using ultrasound image feedback," in *Proc. IEEE Int. Conf. Robot. Automat.*, 2017, pp. 6156–6161.

[39] A. J. Petruska and B. J. Nelson, "Minimum bounds on the number of electromagnets required for remote magnetic manipulation," *IEEE Trans. Robot.*, vol. 31, no. 3, pp. 714–722, Jun. 2015.

[40] K. M. Anstreicher, "Semidefinite programming versus the reformulation-linearization technique for nonconvex quadratically constrained quadratic programming," *J. Global Optim.*, vol. 43, no. 2–3, pp. 471–484, 2009.

Federico Ongaro received the Master's degree (with honors) in automation engineering from the University of Bologna, Bologna, Italy, in 2014, and the Master's degree in control theory and control engineering from the Tongji University, Shanghai, China, in 2015. He is currently pursuing the Ph.D. degree in the field of surgical robotics at the University of Twente, Enschede, The Netherlands.

During his studies, he was awarded the Almatong Academic Scholarship in 2014. His research interests include microrobotics, mechatronic design, control engineering, software design, and electromagnetism.

Stefano Pane was born in Naples, Italy, in 1991. He received the Bachelor's degree in electronic engineering from the University of Roma3, Rome, Italy, in 2015, and the M.Sc. degree (with honors) in mechatronics engineering from the Politecnico di Torino, Turin, Italy, in 2017.

His research interests include biomechatronics and microrobotics.

Stefano Scheggi received the M.Sc. and Ph.D. degrees in computer engineering from the University of Siena, Siena, Italy, in 2007 and 2012, respectively.

In 2011, he was a Visiting Ph.D. Student with the Department of Computer Science, George Mason University, Fairfax, USA, under the supervision of Prof. Jana Kosecka. Since 2012, he held a Postdoctoral position with the University of Siena, Siena, Italy. Since 2015, he holds a Postdoctoral position with the University of Twente, Enschede, The Netherlands. His research interests include computer vision, medical robotics, haptics, and augmented/virtual reality.

Sarthak Misra (S'05–M'10) received the Master's degree from the McGill University, Montreal, QC, Canada, in 2001, and the Doctoral degree from the Johns Hopkins University, Baltimore, MD, USA, in 2009, both in mechanical engineering.

He is currently a Professor with the Department of Biomechanical Engineering, University of Twente, Enschede, The Netherlands, and also with the Department of Biomedical Engineering, University of Groningen and University Medical Center Groningen, Groningen, The Netherlands. Prior to commencing his studies at Johns Hopkins University, he was a Dynamics and Controls Analyst on the International Space Station Program for 3 years. His research interests include surgical robotics and medical microrobotics.

Dr. Misra was the recipient of the European Research Council Starting and Proof-of-Concept Grants and the Netherlands Organization for Scientific Research VENI and VIDI Award. He is a Co-Chair of the Robotics and Automation Society Technical Committee on Surgical Robotics and a Co-Chair of the International Federation of Automatic Control Technical Committee on Biological and Medical Systems.